



High response to sub-ppm level of NO₂ with 50%RH of ZnO sensor obtained by an auto-combustion method

M. Benamara¹ · J. Massoudi² · H. Dahman¹ · E. Dhahri² · L. El Mir¹ · A. Ly³ · M. Debliquy⁴ · D. Lahem³

Received: 8 May 2020 / Accepted: 8 July 2020 / Published online: 20 July 2020
© Springer Science+Business Media, LLC, part of Springer Nature 2020

Abstract

Pure zinc oxide was prepared by a simple auto-combustion method. The microstructure and morphological properties, of the prepared sample, were investigated by XRD, XPS, and SEM characterizations which indicated that the ZnO nanoparticles have a hexagonal wurtzite structure with space group P63mc. The average size estimated by Willams-Hall exhibits to be 61.45 nm which is in good agreement with that estimated by the SEM image (62 nm). The absorbance spectra indicated a high absorbance in the UV range and the gap energy, estimated by Tauc's model, was 3.17 eV. The sensor was prepared by spraying the suspension of ZnO nanopowders on an alumina substrate with pre-deposited gold-interdigitated electrodes. The fabricated sensors exhibited a high response ($\Delta R/R = 208$) and acceptable response/recovery times (5/2.5 min) to 1 ppm of NO₂ at low operational temperature (150 °C) in the dark and 50%RH.

1 Introduction

Nitrogen dioxide (NO₂) is one of the main air pollutants that cause photochemical smog and acid rain. NO₂ is produced by the combustion of gas, coal, wood, or petroleum for domestic and industrial use. We need a high performance NO₂ sensor for detecting or monitoring the concentration level of NO₂ in the atmosphere [1]. Until now, there have been several researchers who have developed different NO₂ sensors such as electrochemical [2, 3] piezoelectric quartz [4], and semiconductor sensors. In the recent years, gas sensors based on semiconductor materials have been become increasingly attractive in the detection of NO₂ due to their low cost, long-term stability, and simplicity of use. The sensors based on several types of metal oxides have been studied such as SnO₂ [4], ZnO [5], WO₃ [6], In₂O₃ [7], CuO [8],

and Fe₂O₃ [9], which exhibit a good performance in NO₂ detection. However, sensors based on semiconductors often work well at high temperatures. This condition needs to be treated due to the energy consumption and unwanted long-term drifting problems caused by the sintering effects in the metal oxide grain boundaries at elevated temperature [10]. Several researchers have reported that zinc oxide is one of the most promising materials for detecting NO₂ gases [11, 12]. ZnO-based gas sensors have an excellent response to NO₂ even at low concentrations. However, to function well, the traditional ZnO-based gas sensors need to be heated to temperatures ranging from 200 to 600 °C [13]. Lowering the operating temperature can not only effectively reduce energy consumption, but also improves safety in the complex atmosphere, especially in flammable gas conditions [14]. In addition, to improve economic efficiency and safety, the development of semiconductor sensors at low temperature or even at room temperature also increases the long-term stability of the sensors [15].

The preparation method is very important to establish the best performance of gas sensors based on semiconductor metal oxides. Zinc oxide has been prepared by several production methods and each method gives different results to others. Kim et al. [16, 17] prove that sensor based on ZnO nanoflowers, prepared by Micropatterning method, had a response value of 29 in 50 ppm NO₂ gas at 270 °C; however, the sensor based on ZnO, prepared by microwave irradiation, gives a response value of 12.57 to 1 ppm level NO₂ gas at

✉ M. Benamara
majdibenamara1@gmail.com

¹ Laboratory of Physics of Materials and Nanomaterials Applied at Environment (LaPhyMNE), Faculty of Sciences in Gabes, Gabes University, 6072 Gabes, Tunisia

² Laboratoire de Physique Appliquée, Faculté des Sciences, Université de Sfax, B. P. 1171, 3000 Sfax, Tunisia

³ Materia Nova, Materials R&D Centre, Parc Initialis, Avenue Nicolas Copernic 3, 7000 Mons, Belgium

⁴ Service de Sciences des Matériaux, Université de Mons, Rue de l'Épargne 56, 7000 Mons, Belgium

300 °C. Jun et al. [18] report that the gas sensor based on ZnO, prepared by patterned thin film and then annealed, has a high NO₂ detection response with rapid recovery and response times at low operating temperature (200 °C). Zhang et al. [19] had prepared ZnO sensor by liquid plasma spray which it gives 9.2 values of response to 1 ppm of NO₂ at high operating temperature (300 °C). Therefore, it is important to find another quality of ZnO powder prepared by a simple and fast method on one hand and we need a low-cost processing protocol which does not require the presence of modern and rare machines on the other hand.

In this study, we have prepared zinc oxide nanopowder by a simple auto-combustion method and then, the as-obtained product was calcined for 7 h at 600 °C. We have investigated the microstructural and morphological proprieties by XRD, XPS, and SEM characterizations. The optical properties were investigated by UV–visible–NIR spectroscopy characterizations. The sensing properties of ZnO sensor towards 0.5, 0.75, 1, 3, and 5 ppm NO₂ gas has been investigated. We have tested ZnO-based sensors at different temperatures and in the dark conditions at which we observed strong responses.

2 Experimental details

2.1 Synthesis

The pure zinc oxide was elaborated by using an auto-combustion method. Dehydrated analytical grade zinc acetate [Zn(CH₃COO)₂ × 2H₂O; 99%] and glycine (NH₂CH₂COOH) were completely dissolved in distilled water until a homogeneous solution was obtained. Glycine

was used as fuel with a ratio (1:2) taken according to the stoichiometry proportion of zinc acetate. Then, the solution was stirred under room temperature about 1 h until uniform solution is obtained. The mixed precursor solution was evaporated on a hot plate at 80 °C with constant magnetic stirring and concentrated by heating until the excess of free water was evaporated with the formation of a viscous gel. The gel obtained was inflamed by raising the temperature to 300 °C. After that, burned powder samples were observed. The burnt powder was treated for 7 h at 600 °C. Finally, the synthesized nanopowders were ground for 1 h. Figure 1 shows the stages of the preparation protocol. This protocol is further explained by Irshad et al. [20]

2.2 Characterization

We have measured the crystalline structure, particle size, morphology, and optical proprieties by the following measurements: X-ray diffraction (XRD); scanning electronic microscopy (SEM); UV–Visible–NIR spectroscopy; and X-ray photoelectron spectrometry (XPS). The crystal structure and the morphological properties of the prepared ZnO powder were observed by X-ray diffractometer (XRD, D8 Advance, Bruker AXS, Germany) and field-emission scanning electron microscopy (FE-SEM, S4800II, Hitachi, Japan), respectively. The phase constitution of the synthesis nanopowders was obtained by X-ray photoelectron spectroscopy (XPS, ESCALAB 250Xi, Thermo Scientific, USA). We have used UV–Vis–NIR spectrophotometer (Shimadzu UV-3101PC) in the wavelength range of 200 to 1800 nm to determine the light absorption properties.

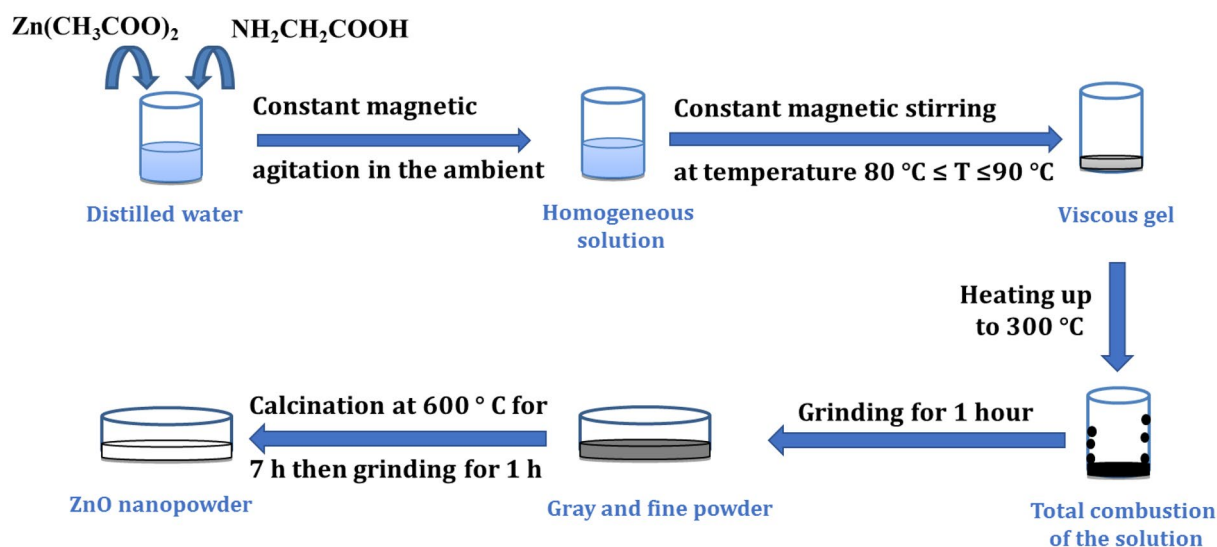


Fig. 1 Preparation protocol

2.3 Fabrication of the sensors

We have dispersed 250 mg of the prepared nanopowders in 2.25 ml of distilled water. Then, the prepared suspension was dispersed by a probe-type Ultrasonicator until a uniformly dispersed solution is obtained. The homogeneous dispersion was deposited by spraying on alumina substrates (Al_2O_3) equipped with a pair of interdigitated gold electrodes and Pt heating elements on the back side (C-MAC Micro Technology Company, Belgium), as shown in Fig. 2. Before sensing tests, the fabricated sensors were calcined for 1 h at 400 °C in air to stabilize the deposited layer.

2.4 Sensing tests

The purpose of this work is to study the response of sensors based on the same material at high temperatures and at room temperature with light assistance. The sensing tests were carried out by measuring the variation of the electrical resistances between air and the target gas. The gas system containing a teflon chamber (Fig. 2) which it was contained the prepared sensor. The gas cylinders are controlled by flowmeters and an electrical system to operate the sensors at a controlled temperature and perform resistance measurements while varying the concentration of the target gas. Before the test, a commercial synthetic air (79% N_2 + 21% O_2) is injected into the chamber until the electrical resistance becomes stable (~2 h). After that, commercial NO_2 gas (balance gas is air) is introduced into the chamber to get the desired NO_2 concentration of 0.5, 0.75, 1, 3, and 5 ppm. After 15 min of injection, the NO_2 gas is removed. These tests were carried out in 50% relative humidity at 22 °C. The response of the gas is defined as the ratio $R = (R_{\text{NO}_2} - R_{\text{air}})/R_{\text{air}}$, where R_{NO_2} and R_{air} are the electrical resistance by 50% relative humidity of the sensor at different NO_2 gas concentrations and in air, respectively. The response and recovery times were evaluated at 90% of

the resistance change after exposure to the target gas and air, respectively.

3 Characterization

3.1 Sample microstructure and morphology

The X-ray diffraction pattern of the ZnO nanopowder was refined by using Rietveld analysis of fullprof's program [21] and was shown in Fig. 3a. The values of the various structural parameters have been calculated and listed in Table 1. The refined network parameters obtained confirm the formation of ZnO under the hexagonal wurtzite structure with reticular plans (100), (002), (101), (102), (110), (103), (200), (112), and (201) and space group P63mc which corresponds to the standard JCPDS data card n°00-005-0664 [22]. The existence of several diffraction peaks indicates the polycrystalline compound. The average size of the crystallites (D_{sc}) was calculated by using the following equation of Debye–Scherrer [23]. The obtained D_{sc} value is 44 nm as presented in Table 1. The goodness of fit (χ^2) was a low value which suggests that the refining of the sample is effective and that the sample obtained was of better quality. The unit cell volume for a hexagonal system was calculated from the following equation: [24]

$$V = 0.866 \cdot a^2 \cdot c \quad (1)$$

The wurtzite structure has a hexagonal unit cell with two network parameters, a and c , and a ratio $c/a = 1.633$. The deviation of the crystal from the perfect arrangement can be calculated by expressing the degree of distortion $R = 1.633 a/c$, where $R = 1$ gives an ideal wurtzite structure with $c/a = 1.633$ [24]. In addition, the size of the crystallites and the lattice strain of ZnO particles were evaluated by using Williamson-Hall method [25]. Representative plots of a Williamson-Hall

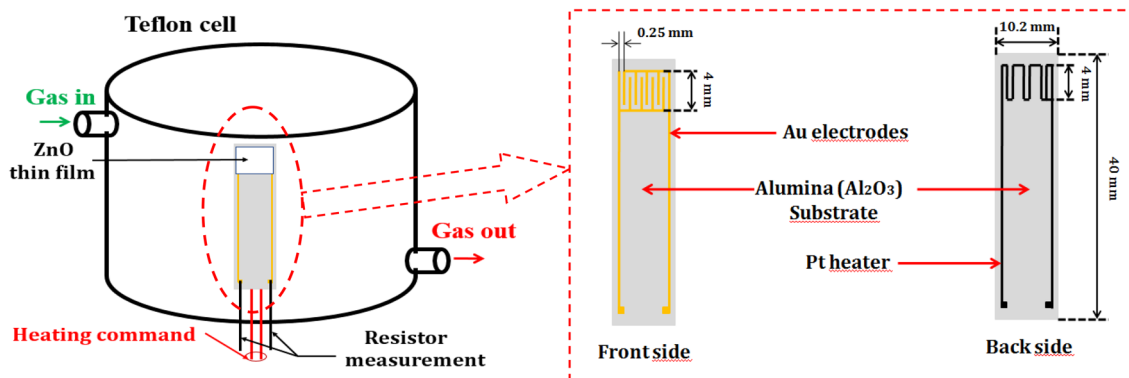


Fig. 2 Scheme of test chamber and ZnO sensor substrate

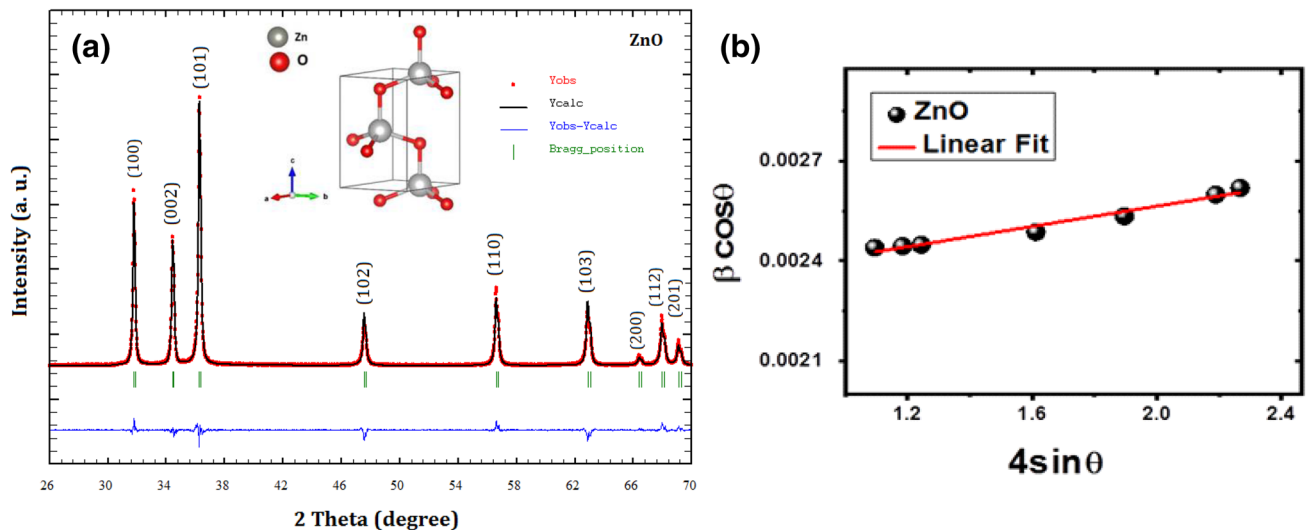


Fig. 3 **a** Rietveld refinement of the X-ray diffraction pattern and **b** Williamson–Hall plot for ZnO prepared by auto-combustion method

Table 1 Lattice constant (a , c), unit cell volume (V), Rietveld refinement parameters, specific surface area (S), X-ray density ($\rho_{X\text{-ray}}$), and crystallite size

a (Å)	3.2493
c (Å)	5.2049
V (Å ³)	47.589
c/a	1.6018
R	0.9999
χ^2	1.81
R_p (%)	8.87
R_{wp} (%)	11.0
R_e (%)	8.19
S (m ² /g)	12
$\rho_{X\text{-ray}}$ (g cm ⁻³)	11.3583
D_{sc} (nm)	44
D_{WH} (nm)	61.35
$\varepsilon \times 10^{-5}$	89
D_{SEM} (nm)	62

sample of ZnO is shown in Fig. 3b. The curve of $\beta\cos\theta$ as a function $4\sin\theta$ provides the strain through the slope of the line and the size of the particles (D_{WH}) can be evaluated from the interception of the line. Table 1 shows that the average size of the crystallites estimated from the Scherrer equation is very different from that obtained by W–H plot. This difference can be explained by the presence of the fact micro-stress, by which it can induce a larger widening of the diffraction peak, whereas, in the Scherrer equation, the total width of the diffraction peak is taken into account in the calculation. The microtension of the network as the sample obtained using the Williamson-Hall method displays a positive value which indicates the existence of a small microtension in the crystalline network. We have studied the morphology of the ZnO samples by SEM analysis and the frequency as a function of the particle

size which we can esteem as the average grain size. These results are shown in Fig. 4. The obtained image indicates the presence of agglomerates composed by a non-uniform distribution of grains in spherical form and of average size equal to 62 nm. Table 1 presents the crystallite and the grain size of the ZnO sample deduced from the XRD and SEM investigations, respectively. By comparison with the particle size values estimated from SEM, the average particle size agrees with the average particle size estimated from the W–H model. In the present study, we can conclude that the model of Williamson-Hall is the most suitable method than the Scherrer formula. In addition, we can conclude that each sample grain is almost monocrystalline in nature. By considering that a basic unit cell of the cubic spinel structure contained eight ions, the X-ray density ($\rho_{X\text{-ray}}$) of the sample can be calculated by using the following equation [25]:

$$\rho_{X\text{-ray}} = \frac{4 \cdot M}{N_A \cdot V} \quad (2)$$

where “ N_A ” is Avogadro’s number, “ M ” is the molecular weight of each compound, “ v ” is the volume, and 4 represent the number of molecules in a unit cell of the hexagonal wurtzite lattice. This can explain to us that the density of X-rays is directly linked to the molar mass and inversely linked to the unit cell volume of the material. If all the particles are spherical, the specific surface has been calculated from the relation [25]:

$$S = \frac{6000}{D \cdot \rho_{X\text{-ray}}} \quad (3)$$

where the constant 6000 is called form factor for spherical particles, “ $\rho_{X\text{-ray}}$ ” is the X-ray density, and D is the diameter

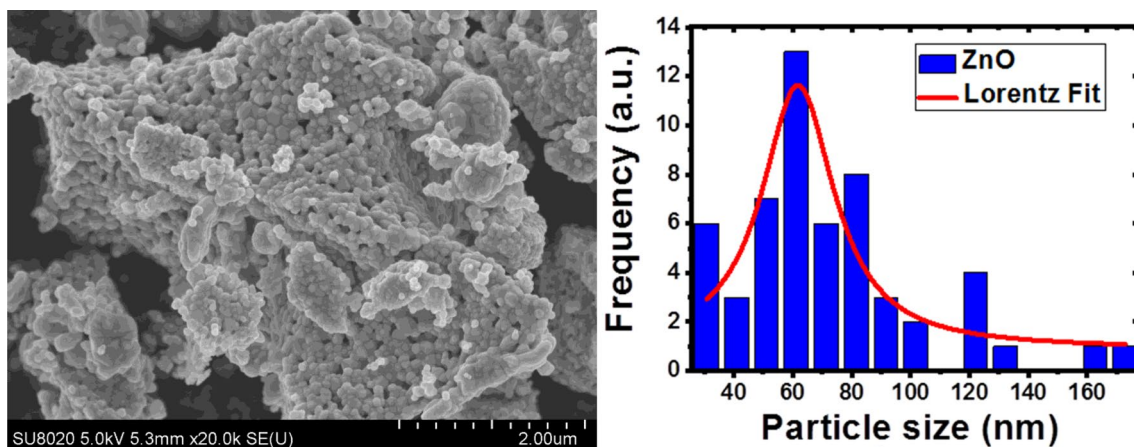


Fig. 4 SEM image of ZnO sample prepared by auto-combustion method

of the particle. The auto-combustion method is known to synthesize nanopowders with high specific surface area (S). The specific surface area of ZnO nanoparticles has a high value ($12 \text{ m}^2/\text{g}$) which is needed for sensing application [26–28].

We have investigated the X-ray photoelectron spectroscopy (XPS) of the ZnO sample to have information about elemental identification of the constituents in the surface region. The core levels of C 1s, O 1s, and Zn 2p are detected and shown in Fig. 5a–c, respectively. Generally, the binding energies of 284.6 of C 1s are used as internal references in the spectrum [29]. The spectra corresponding to the O 1s and the Zn 2p3 spectra of the ZnO_{1-x} samples are calibrated by the binding energy of the C 1s (284.6 eV) as an internal reference spectrum [30]. The Zn 2p3 spectrum exhibits a located peak at 1021.1 eV, corresponding to the 2p 3/2. It confirms the existence of the ions Zn^{2+} in the composites. The O1s signal deconvoluted into three subcomponents at 528.33, 529.87, and 531.16. The peak of 531.16 eV (at high banding energy) is associated with defective oxygen and the signal 529.87 eV is assigned to the oxygen network in the hexagonal structure of ZnO [31, 32]. We know that the O 1s peaks are strongly influenced by the oxidation state of ZnO. In Fig. 5c, we have seen that the intensity of the defective oxygen peak has a significant value, which means that there are oxygen vacancies in the sample. Xu et al. have proven that oxygen vacancies are easily created in metal oxides during the hydrothermal process [33–35]. We can conclude from the core levels of Zn and O that there are rich double-donor defects (interstitial of Zn and vacancy of O) in our sample [36].

3.2 UV–visible–NIR characterization

We have studied the optical properties of pure zinc oxide by UV–Visible–NIR absorption and reflectance spectra

measurements in the range 200–1800 nm and the results are presented in Fig. 6a, b, respectively. We have investigated that a high absorbance appears in the UV range (200–400 nm), but for the wavelengths higher than 400 nm, we have observed a remarkable increasing of the absorbance in the visible and near-infrared ranges. This result is confirmed by the optical diffuse reflectance of ZnO nanopowders measured at room temperature. The reflectance has a value under 4% in the UV range which shows that absorption is highest in this region. In contrast, the reflectance has more than 80% in the Visible-NIR light region, which indicates that the optical diffusion power of this type of material is important in this range. We have studied the variation of $(\alpha h\nu)^2$ as a function photon energy (Fig. 6a), which it was according to Tauc's law relationship [37, 38]. The gap energy of ZnO, estimated from Tauc's plot, was equal to 3.17 eV. To confirm this result, the energy of the band gap is estimated using the first derivative of the reflectance ($dR/d\lambda$) [39, 40]. The spectrum of variation of the first derivative of the reflectance ($dR/d\lambda$) as a function of the wavelength (λ) for the ZnO nanopowders is illustrated in the inset of Fig. 6b. The estimated value of the gap energy of this method is very close to that estimated by Tauc's law. The value of the band gap is corresponding to the wavelength of value 391 nm.

3.3 NO₂ sensing tests

The gas detection characteristics of a ZnO thin layer, thickener $\sim 10 \mu\text{m}$, have been studied in the NO₂ concentration range from 0.5 to 5.0 ppm as target gas using various working temperatures from 100 to 350 °C in the dark. Fig. 7a shows the resistances of the ZnO sensor as a function of time at different temperatures and under different concentrations of NO₂. The resistance under air was decreased when the operating temperature was increased. Under the exposure of NO₂ gas, the resistance of the ZnO sensor has been increased

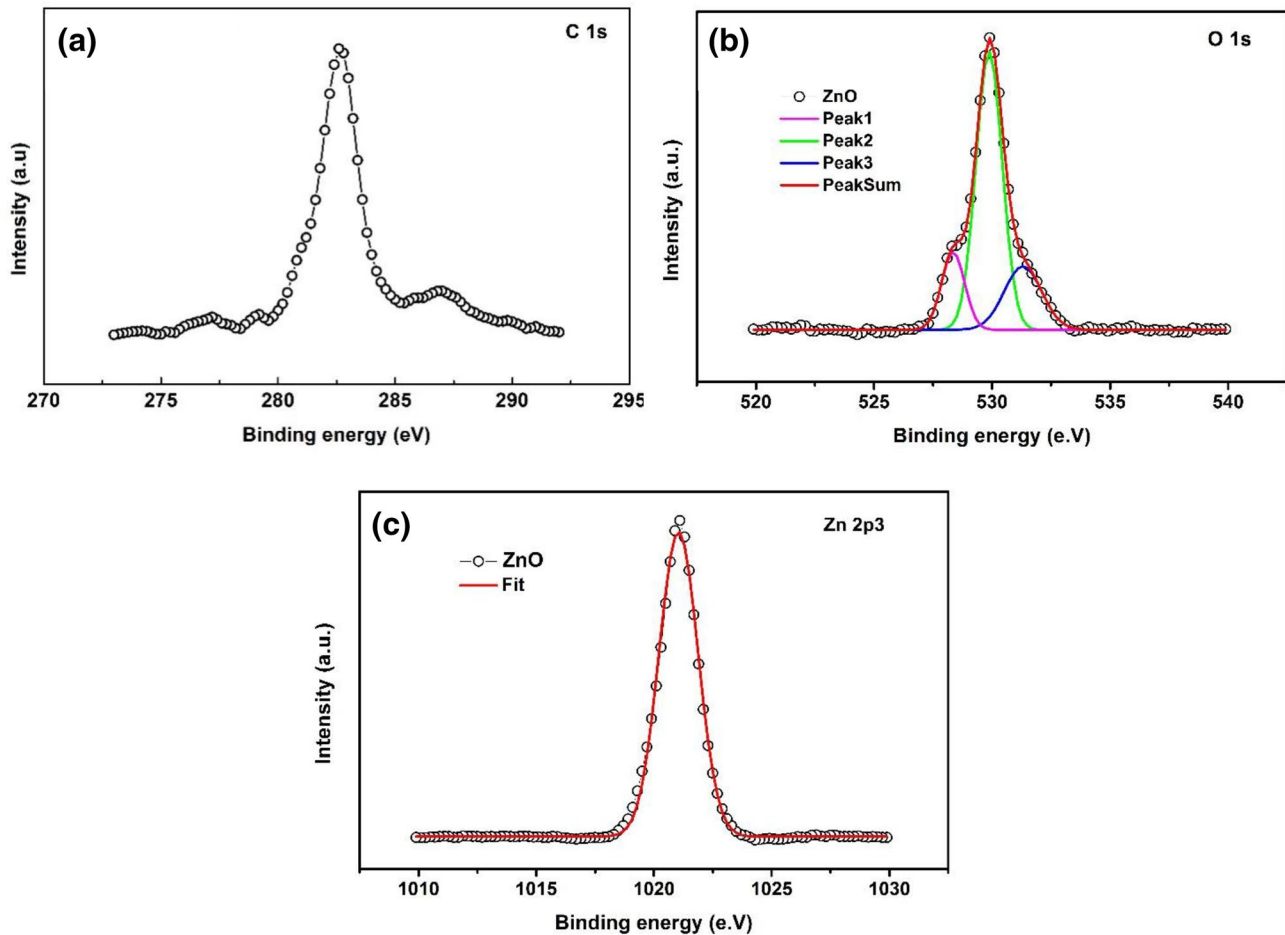


Fig. 5 XPS spectra **a** C 1s, **b** O 1s, and **c** Zn 2p3 of the ZnO sample

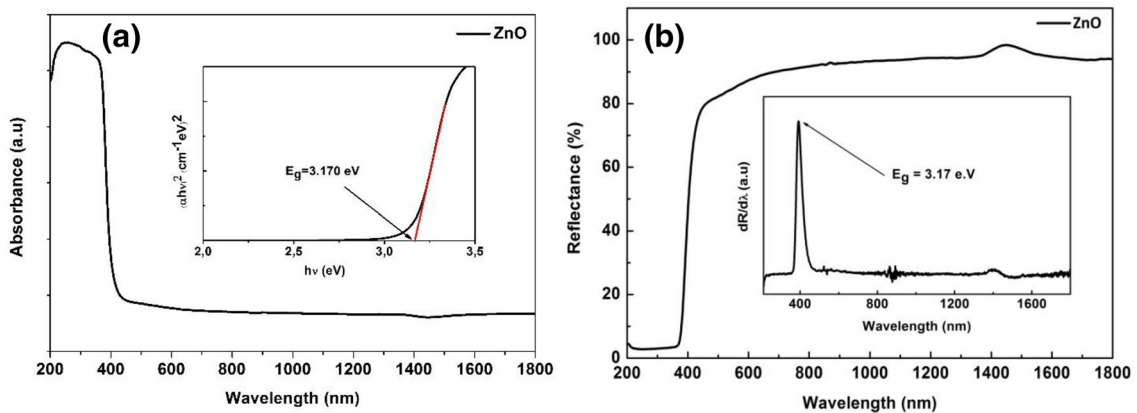


Fig. 6 **a** Absorbance and **b** reflectance spectra of ZnO sample prepared by auto-combustion method

whatever the operating temperature which indicates that our material is sensitive to NO_2 molecules. The transient response curves, between 0.5 and 5.0 ppm of NO_2 concentration, as a function of operating temperature indicate better

performance of the sensor in the operating temperature ranging from 100 to 200 °C, as shown in Fig. 7b. In particular, we have seen the best response at 150 °C which is reached approximately 200 times to 1 ppm of NO_2 . The response/

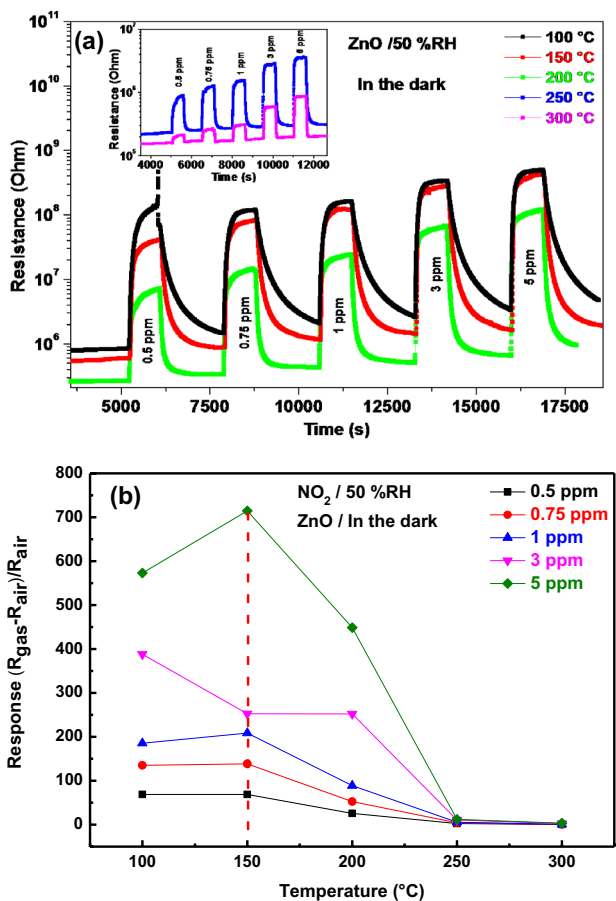


Fig. 7 a ZnO sensor resistance versus time under different temperature and b ZnO sensor response versus operational temperature under different concentration of NO₂ gas

recovery times, presented in Table 2, were slow at the operating temperature below 200 °C. For an optimal temperature of 150 °C, the response time of 5 min and the recovery time of 2.5 min of the device dramatically decreased when the operating temperature was 300 °C. It is clear in Fig. 7b that the NO₂ sensing response is better at a working temperature of 150 °C whatever the gas concentration. However, the response of the sensor decreases at temperatures of 250 °C

Table 2 Response and response/recovery times versus temperature of ZnO in 1 ppm of NO₂ under dark condition and 50% of humidity

Temperature (°C)	R _{air} (Ω)	Response $(R_{NO_2} - R_{air})/R_{air}$	Response time (min)	Recovery time (min)
100	8.36×10^5	185.6	6.9	6.4
150	5.96×10^5	208.5	5	2.5
200	2.69×10^5	89.1	9	1.5
250	2.33×10^5	5.6	3.3	1.4
300	1.60×10^5	0.9	2.6	0.6

and 300 °C. This means that at higher temperatures the sensitivity of the sensor based on ZnO decreases. This may be due to the atomic oxygen species which compete with the NO₂ gas molecules for the energy sites on the surface of the metal oxide [41]. The transient response of the ZnO sample, under different concentrations of NO₂ arranged between 0.5 and 5.0, was studied at the optimal temperature of 150 °C. This low operating temperature is linked to the small gap energy value ($E_g = 3.17$ eV) of this present material comparing against zinc oxide elaborated by other techniques ($E_g \approx 3.3$ eV). The results are presented in Fig. 8. In Fig. 8, the response value of ZnO sensor was increased to 72, 139, 208, 478, and 713 as the concentration of NO₂ increased from 0.5, 0.75, 1, 3, and 5 ppm, respectively. This is due to the high fundamental specific surface which is 12 m²/g.

The ZnO sensor responses toward other tested gases, such as NO₂, acetone, ethanol, and formaldehyde, at the same temperature of 150 °C were investigated and presented in Fig. 9. These results indicate that the ZnO sensor exhibits an ultra-high response 208 to 1 ppm of NO₂ concentration. The responses to other environmental gases for 5 ppm of concentration is very low (under 15), indicating a good selectivity toward NO₂.

The pure zinc oxide has been prepared by simple auto-combustion method and was tested to NO₂ gas under different temperatures in the dark condition. Table 3 presents our NO₂ gas sensor-based ZnO, at a low operational temperature of 150 °C; compared to the other ZnO sensor prepared by other production methods, this sensor presented had an ultra-high response to NO₂ gas at ppm levels, the more it was the lower the response and recovery time than other sensors. Jun et al. [18] obtained higher response of 400 towards 5 ppm NO₂ gas in operating temperature of 200 °C and the response and recovery times were respectively 0.17 and 0.22 min with

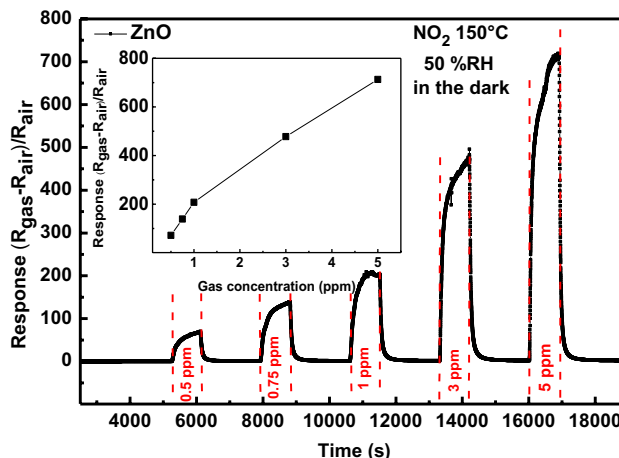


Fig. 8 Sensor response versus time in 0.5, 0.75, 1, 3, and 5 ppm of NO₂ gas concentrations at 150 °C under dark

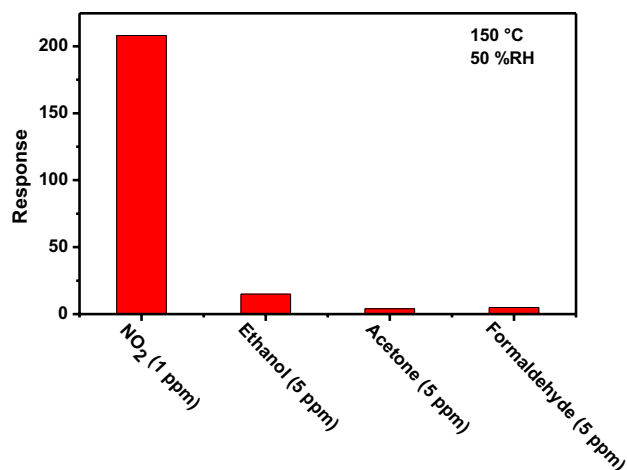


Fig. 9 Selectivity of ZnO-based sensor to various gases at 150 °C and 50%RH

no used activation light. Compared with our case, we have an ultra-high response of 713 towards 5 ppm NO₂ gas in 150 °C operating temperature. ZnO prepared by Zhang et al. [19], ZnO/graphene nanocomposites synthesized by Kim et al. [17], and AZO-2 elaborated by Y. H. Zhang [44] have been tested to 1 ppm NO₂ which indicate responses of 9.2 in 300 °C, 12.57 in 300 °C, and 103.98 in 240 °C, respectively. The other studies, presented in Table 3, of pure and doped ZnO found responses less than 30 to high NO₂ concentrations (more than 10 ppm) at high functional temperatures (more than 200 °C).

3.4 Sensing mechanism

The detection mechanism of the ZnO sensor is explained by the change in conductivity caused by the chemical reaction between the adsorbed oxygen and the gas to be detected on the surface of the sensor material. During crystal growth,

there may be a small number of intrinsic oxygen defects (oxygen vacancies) produced. Those oxygen vacancies act as donor levels releasing electrons in the conduction band. Sub-stoichiometries ZnO is a n-type semiconductor. Secondly, the oxygen vacancies act as preferential adsorption sites for the oxygen molecules from the air and subsequently combine with electrons on the ZnO conduction band to form ionized O₂⁻, O⁻, and O²⁻ species according to following reactions:



The ionized O₂⁻, O⁻, and O²⁻ species are dominant below 150 °C, between 150 and 300 °C, and above 300 °C, respectively [46]. The principle of absorption of oxygen on the sensor surface was more explained in Fig. 10. The oxygen species adsorbed on the surface of ZnO are mainly O⁻ at 150 °C, and a depletion zone is formed due to the electrons trapped by the oxygen (Fig. 11). As the sensitive layer is made of small grains, the electrons have to jump through a potential barrier between the grains. The global resistance of the deposited layer being linked to the sum of the resistances of the contacts between the ZnO grains. The conductance for this kind of structure can be expressed as follows:

$$G = G_0 \exp\left(-\frac{e \cdot V_s}{k_B \cdot T}\right) \quad (7)$$

Equation (7) shows the role of the potential barrier which is of course directly linked to the amount of adsorbed molecule per surface unit. Currently, a major problem with semiconductor gas sensors at room temperature is kinetics: response and

Table 3 Performance of ZnO as 150 °C of temperature NO₂ sensor in comparison with ZnO literature results

Materials	Fabrication method	Sensing temperature (°C)	NO ₂ (ppm)	Response	Response/recovery times (min)	References
ZnO	Patterned thin film and annealing	200	5	400	1.68/0.9	[18]
ZnO/CuO NWs	Hydrothermal	350	10	30	4.16/5.67	[42]
ZnO	Liquid plasma spray	300	1	9.2	8.7/over 20	[19]
DF-ZnO Nanoflowers	Micropatterning technique	270	50	29	0.42/0.47	[16]
ZnO/graphene Nanocomposites	Microwave irradiation	300	1	12.57	2.13/1.42	[17]
Al:ZnO	Sol-gel	200	100	18.5	0.13/2.01	[43]
AZO-2	Hydrothermal	240	1	103.98	0.88/0.35	[44]
AZO hollow nanofiber	Sputtering	250	0.5	10.74	0.38/0.42	[45]
ZnO	Auto-combustion	150	1	208.5	5/2.5	This work

Fig. 10 Principle of adsorption of oxygen on the surface of the ZnO-based sensor

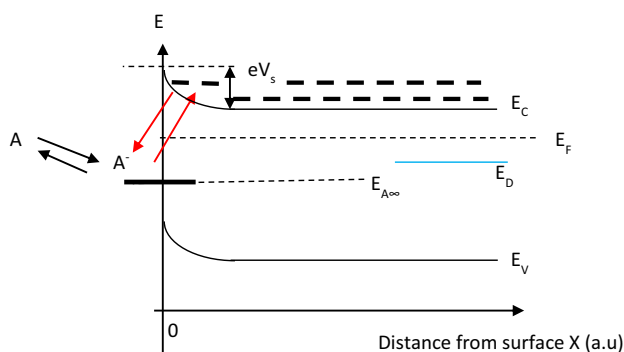
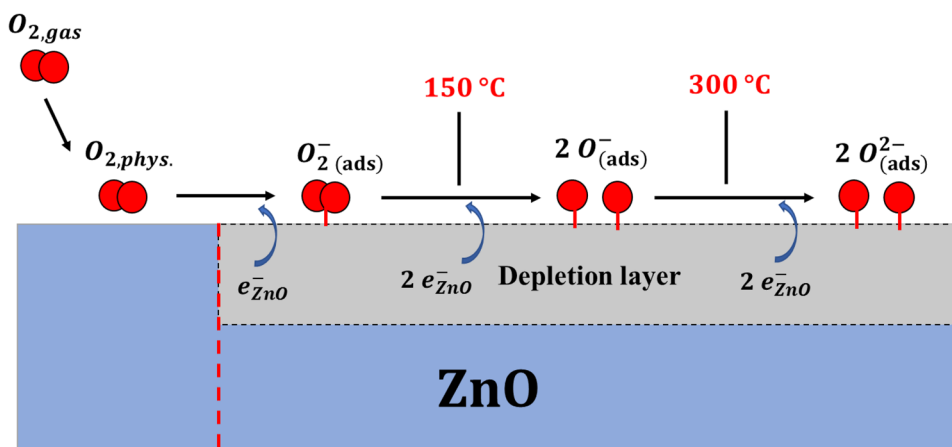


Fig. 11 Scheme of the effect of the adsorption of an acceptor molecule (like oxygen) on the surface of the semiconductor

recovery rates. Response and recovery times are very long because we are dealing with chemical adsorption phenomena that are activated. Taking Langmuir’s adsorption model as a first approach (Wolkenstein’s model considering the electron transfers is more adapted), we may write the following:

If N is the surface concentration in adsorption sites, the surface coverage can be defined as the fraction of sites occupied by the adsorbate.

$$\theta = \frac{[X^*]}{N} \tag{8}$$

$$\frac{d\theta}{dt} = r_{ads} - r_{des} \tag{9}$$

$$r_{ads} = K_{ads} \cdot (1 - \theta) \cdot p \tag{10}$$

$$r_{des} = K_{des} \cdot \theta \tag{11}$$

Times of adsorption and desorption are expressed [47] as follows:

$$\tau_{ads} = \frac{1}{K_{ads} P_A + K_{des}} \tag{12}$$

$$\tau_{des} = \frac{1}{K_{des}} \tag{13}$$

where K_{ads} , K_{des} , and P_A are the adsorption coefficient, the desorption coefficient, and the partial gas pressure, respectively. In this case, P_A is a constant. The adsorption and desorption times are inversely proportional to K_{ads} and K_{des} , respectively. So that, increasing K_{ads} and K_{des} exhibit decreasing τ_{ads} and τ_{des} . K_{ads} and K_{des} are determined by the following expressions:

$$K_{ads} = K_{ads}^0 \exp\left(\frac{-E_{ads}}{k_B T}\right) \tag{14}$$

$$K_{des} = K_{des}^0 \exp\left(\frac{-E_{des}}{k_B T}\right) \tag{15}$$

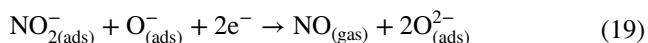
where k_B and T are Boltzmann constant and the temperature; E_{des} and E_{ads} are the desorption and adsorption activation energies, respectively; and K_{des}^0 and K_{ads}^0 are adsorption and desorption constants, respectively. We can see that the coefficients K_{ads} and K_{des} mainly depend on the temperature and increase with increasing temperature, which can explain the decrease of the response and recovery times with increasing the temperature in the test of the ZnO sensor at different temperatures (Table 2). At equilibrium, we can express the surface fraction occupied by the gas θ by the following equation

$$\theta = \frac{K P_A}{K P_A + 1} \tag{16}$$

where K is the adsorption constant and is expressed as follows:

$$K = \frac{K_{ads}}{K_{des}} = \frac{K_{ads}^0}{K_{des}^0} \exp\left(\frac{Q_{ads}}{k_B T}\right), \text{ which } Q_{ads} = E_{des} - E_{ads} \tag{17}$$

The response to gas is linked to θ . Of course, the higher the adsorption heat, the higher the surface coverage. When NO_2 is injected, NO_2 molecules can adsorb on the surface and capture electrons from the ZnO conduction band (CB) to form NO_2^- species (Eq. 18), which could further increase the height of the barrier potential at the surface and therefore cause an increase in electrical resistance of the material (Fig. 12). O^- from the surface of the material can combine with NO_2 gas to form NO and O^- (Eq. 19). The reactions, that are produced in this process, are as follows: [16, 48]



The band structure is shown in Fig. 13. During the contact of ZnO with NO_2 , electrons are captured from the conduction band at the surface which will increase the potential barrier (P.B.) at the surface because the electron

affinity of NO_2 is bigger than that of oxygen ($E_a = 0.48$ eV for O_2 , $E_a = 2.04$ eV for NO_2) and the trap is deeper [49], causing more electrons captured from the conduction band to form NO_2^- and NO species resulting in an increase of the sensor resistance [50]. When NO_2 is injected, a competition takes place on the surface of the semiconductor with the already adsorbed oxygen. As oxygen at low temperature desorbs slowly, its replacement with NO_2 can take a long time. That is why the response is slow and lower. Also, the recovery is slow because desorption is slow. The adsorption phenomenon is exothermic and the adsorption constant decreases with temperature. That is why the response decreases for high temperatures.

4 Conclusion

In this study, we prepared ZnO by auto-combustion method. The measurement by X-ray diffraction indicated the polycrystalline material and the structure of hexagonal wurtzite with space group P63mc. The average crystallites size was estimated by two methods: Scherrer and Williamson-Hall which are 44 and 61.35 nm, respectively. Consequently, the crystallites are nanometric. Morphological study by SEM

Fig. 12 Schematic of the gas sensing process in air and in NO_2

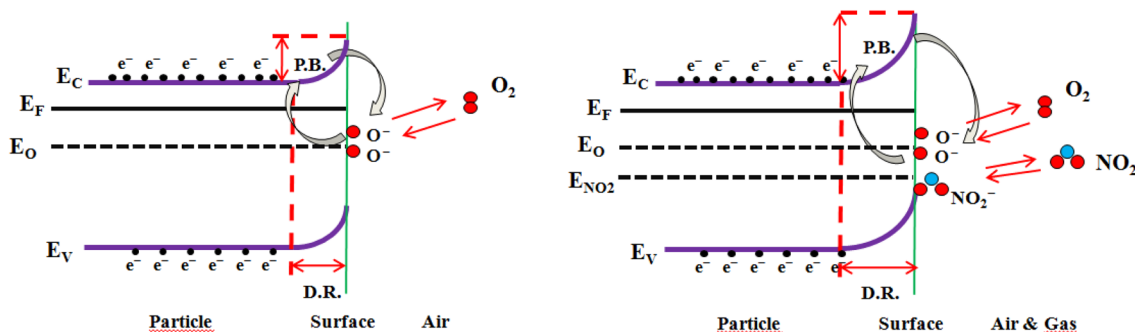
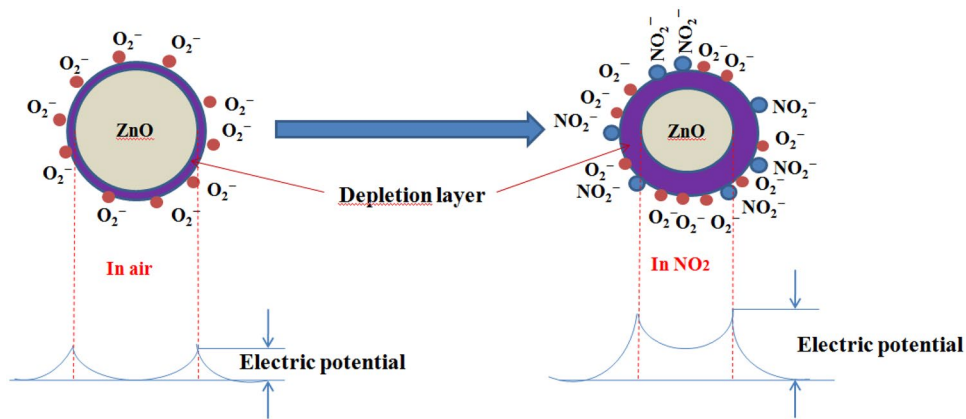


Fig. 13 Schematic of the gas sensing process of ZnO in 150 °C in the dark

analysis indicated the presence of hexagonal agglomerates made up of nanometric particles as it has an average size 62 nm. The absorption spectra in the UV–Vis–NIR range highlighted higher absorption in the UV range of ZnO powder. The band gap energy which was determined by Tauc's law model is equal to 3.170 eV. The sensing test of ZnO sensor at different measurement temperatures in dark for 0.5, 0.75, 1, 3, and 5 ppm of NO₂ concentrations was investigated. It was indicated that the sensor exhibits a high response at low operational temperature of 150 °C and acceptable response/recovery times compared to the results obtained in the literature of ZnO elaborated by other methods. In addition, this sample is selective for all gas used in the present work.

Acknowledgements This work is financially supported by the Tunisian Ministry of Higher Education and Scientific Research (PRF 2019-D4P2), the European Regional Development Fund (ERDF), and the Walloon Region of Belgium through the Interreg V France-Wallonie-Vlaanderen program, under PATHACOV project and the Micro + project co-funded by the European Regional Development Fund (ERDF) and Wallonia, Belgium (No. 675781-642409).

References

- J. Tamaki, High sensitivity semiconductor gas sensors. *Sens. Lett.* **3**, 89–98 (2005)
- C.O. Park, J.W. Fergus, N. Miura, J. Park, A. Choi, Solid-state electrochemical gas sensors. *Ionics* **15**, 261–284 (2009)
- J.W. Fergus, Materials for high temperature electrochemical NO_x gas sensors. *Sens. Actuators B* **121**, 652–663 (2007)
- W.P. Carey, B.R. Kowalski, Chemical piezoelectric sensor and sensor array characterization. *Anal. Chem.* **58**, 3077–3084 (1986)
- J. Tamaki, Y. Okochi, S. Konishi, Effect of oxide-electrode interface on dilute NO₂ sensing properties of WO₃ thin film nanosensors. *Electrochemistry* **74**, 159–162 (2006)
- V.V. Plashnitsaa, V. Guptab, N. Miurac, Mechanochemical approach for fabrication of a nano-structured NiO-sensing electrode used in a zirconia-based NO₂ sensor. *Electrochim. Acta* **55**, 6941–6945 (2010)
- P.C. Xua, Z.X. Cheng, Q.Y. Pan, J.Q. Xu, Q. Xiang, W.J. Yu, Y.L. Chu, High aspect ratio In₂O₃ nanowires: synthesis, mechanism and NO₂ gas-sensing properties. *Sens. Actuators B* **130**, 802–808 (2008)
- A. Kolmakov, X.H. Chen, M. Moskovits, Functionalizing nanowires with catalytic nanoparticles for gas sensing application. *J. Nanosci. Nanotechnol.* **8**, 111–121 (2008)
- Y. Zhang, A. Kolmakov, Y. Lilach, M. Moskovits, Electronic control of chemistry and catalysis at the surface of an individual tin oxide nanowire. *J. Phys. Chem. B* **109**, 1923–1929 (2005)
- G. Lu, J. Xu, J. Sun, Y. Yu, Y. Zhang, F. Liu, UV-enhanced room temperature NO₂ sensor using ZnO nanorods modified with SnO₂ nanoparticles. *Sens. Actuators B* **162**(1), 82–88 (2012)
- Y. Qin, X. Li, F. Wang, M. Hu, Solvothermally synthesized tungsten oxide nanowires/nanorods for NO₂ gas sensor applications. *J. Alloys Compd.* **509**, 8401–8406 (2011)
- S. Jaballah, M. Benamara, H. Dahman, D. Lahem, M. Debliquy, L. El Mir, Formaldehyde sensing characteristics of calcium-doped zinc oxide nanoparticles-based gas sensor. *J. Mater. Sci.* (2020).
- C. Zou, F. Liang, S. Xue, Synthesis and oxygen vacancy related NO₂ gas sensing properties of ZnO: Co nanorods arrays grown by a hydrothermal method. *Appl. Surf. Sci.* **353**, 1061–1069 (2015)
- C. Han, D. Hong, S. Han, J. Gwak, K. Singh, Catalytic combustion type hydrogen gas sensor using TiO₂ and UV-LED. *Sens. Actuators B* **125**, 224–228 (2007)
- S. Mishra, C. Ghanshyam, N. Ram, R.P. Bajpai, R.K. Bedi, Detection mechanism of metal oxide gas sensor under UV radiation. *Sens. Actuators B* **97**, 387–390 (2004)
- J.W. Kim, Y. Porte, K.Y. Ko, H. Kim, J.M. Myoung, Micropatternable double-faced ZnO nanoflowers for flexible gas sensor. *ACS Appl. Mater. Interfaces* **9**, 32876–32886 (2017)
- H.W. Kim, Y.J. Kwon, A. Mirzaei, S.Y. Kang, M.S. Choi, J.H. Bang, S.S. Kim, Synthesis of zinc oxide semiconductors-graphene nanocomposites by microwave irradiation for application to gas sensors. *Sens. Actuators B* **249**, 590–601 (2017)
- J.H. Jun, J. Yun, K. Cho, I.S. Hwang, J.H. Lee, S. Kim, Necked ZnO nanoparticle based NO₂ sensors with high and fast response. *Sens. Actuators B* **140**, 412–417 (2009)
- C. Zhang, M. Debliquy, H. Liao, Deposition and microstructure characterization of atmospheric plasma sprayed ZnO coatings for NO₂ detection. *Appl. Surf. Sci.* **256**, 5905–5910 (2010)
- K. Irshad, M.T. Khan, A. Murtaza, Synthesis and characterization of transition-metals-doped ZnO nanoparticles by sol-gel autocombustion method. *Phys. B* **543**, 1–6 (2018)
- J. Rodríguez-Carvajal, Recent advances in magnetic structure determination by neutron powder diffraction. *Phys. B* **192**(1–2), 55–69 (1993)
- X. Si, Y. Liu, X. Wu, W. Lei, J. Lin, T. Gao, L. Zheng, Al–Mg co-doping effect on optical and magnetic properties of ZnO nanoparticles. *Phys. Lett. A* **379**, 1445–1448 (2015)
- P. Thompson, D.E. Cox, J.B. Hastings, Rietveld refinement of Debye-Scherrer synchrotron X-ray data from Al₂O₃. *J. Appl. Crystallogr.* **20**(2), 79–83 (1987)
- D.K. Dubey, D.N. Singh, S. Kumar, C. Nayak, P. Kumbhakar, S.N. Jha, D. Bhattacharya, A.K. Ghosh, S. Chatterjee, Local structure and photocatalytic properties of sol-gel derived Mn–Li co-doped ZnO diluted magnetic semiconductor nanocrystals. *RSC Adv.* **6**(27), 22852–22867 (2016)
- D. Bouokkeze, J. Massoudi, W. Hzez, M. Smari, A. Bougoffa, K. Khirouni, L. Bessais, Investigation of the structural, optical, elastic and electrical properties of spinel LiZn₂Fe₃O₈ nanoparticles annealed at two distinct temperatures. *RSC Adv.* **9**(70), 40940–40955 (2019)
- E.R. Kumara, C. Srinivasb, M.S. Seehrac, M. Deeptyb, I. Pradeepe, A.S. Kamzin, M.V.K. Meharg, N.K. Mohanh, Particle size dependence of the magnetic, dielectric and gas sensing properties of Co substituted NiFe₂O₄ nanoparticles. *Sens. Actuators A* **279**, 10–16 (2018)
- A. Benali, M. Bejar, E. Dhahri, M.P.F. Graça, M.A. Valente, A. Radwan, High ethanol gas sensing property and modulation of magnetic and A C-conduction mechanism in 5% Mg-doped La_{0.8}Ca_{0.1}Pb_{0.1}FeO₃ compound. *J. Mater. Sci.* **30**, 12389–12398 (2019)
- H. Trabelsi, M. Bejar, E. Dhahri, M.A. Valente, M.P.F. Graça, Oxygen-vacancy-related Giant permittivity and Ethanol sensing response in SrTiO_{3-d} ceramics. *Physica E* **108**, 317–325 (2019)
- W. Li, G. Wang, C. Chen, J. Liao, Z. Li, Enhanced visible light photocatalytic activity of ZnO nanowires doped with Mn²⁺ and Co²⁺ ions. *Nanomaterials* **7**(1), 20 (2017)
- J. Das, S.K. Pradhan, D.R. Sahu, D.K. Mishra, S.N. Sarangi, B.B. Nayak, S. Verma, B.K. Roul, Micro-Raman and XPS studies of pure ZnO ceramics. *Phys. B* **405**(10), 2492–2497 (2010)
- X. Geng, C. Zhang, Y. Luo, M. Debliquy, Preparation and characterization of Cu_xO_{1-y}@ZnO_{1-α} nanocomposites for enhanced

- room-temperature NO₂ sensing applications. *Appl. Surf. Sci.* **401**, 248–255 (2017)
32. C. Zhang, X. Geng, H. Liao, C. Li, M. Debliquy, Room-temperature nitrogen-dioxide sensors based on ZnO_{1-x} coatings deposited by solution precursor plasma spray. *Sens. Actuators B* **242**, 102–111 (2017)
33. B. Xu, Q. Zhang, S. Yuan, M. Zhang, T. Ohno, Morphology control and characterization of broom-like porous CeO₂. *Chem. Eng. J.* **260**, 126–132 (2015)
34. B. Xu, Q. Zhang, S. Yuan, M. Zhang, T. Ohno, Synthesis and photocatalytic performance of yttrium-doped CeO₂ with a porous broom-like hierarchical structure. *Appl. Catal. B* **183**, 361–370 (2016)
35. B. Xu, Q. Zhang, S. Yuan, S. Liu, M. Zhang, T. Ohno, Synthesis and photocatalytic performance of yttrium-doped CeO₂ with a hollow sphere structure. *Catal. Today* **281**, 135–143 (2017)
36. X. Geng, P. Lu, C. Zhang, D. Lahem, M.G. Olivier, M. Debliquy, Room-temperature NO₂ gas sensors based on rGO@ZnO_{1-x} composites: experiments and molecular dynamics simulation. *Sens. Actuators B* **282**, 690–702 (2019)
37. B. Tiss, M. Erouel, N. Bouguila, M. Kraini, K. Khirouni, Effect of silver doping on structural and optical properties of In₂S₃ thin films fabricated by chemical pyrolysis. *J. Alloy. Compd.* **771**, 60–66 (2019)
38. J. El Ghoul, N. Bouguila, S.A. Gómez-Lopera, L. El Mir, Structural and optical properties of nanoparticles (V, Al) co-doped ZnO synthesized by sol–gel processes. *Superlattices Microstruct.* **64**, 451–459 (2013)
39. R. Henríquez, P. Grez, E. Munoz, H. Gómez, J.A. Badán, R.E. Marotti, E.A. Dalchiele, Optical properties of CdSe and CdO thin films electrochemically prepared. *Thin Solid Films* **518**(7), 1774–1778 (2010)
40. S. Mourad, J. El Ghoul, K. Omri, K. Khirouni, Indium doping effect on properties of ZnO nanoparticles synthesized by sol–gel method. *Chin. Phys. B* **28**(4), 047701 (2019)
41. V.L. Patil, S.A. Vanalakar, N.L. Tarwal, A.P. Patil, T.D. Dongale, J.H. Kim, P.S. Patil, Construction of Cu doped ZnO nanorods by chemical method for Low temperature detection of NO₂ gas. *Sens. Actuators A* **299**, 111611 (2019)
42. K. Diao, J. Xiao, Z. Zheng, X. Cui, Enhanced sensing performance and mechanism of CuO nanoparticle-loaded ZnO nanowires: comparison with ZnO–CuO core-shell nanowires. *Appl. Surf. Sci.* **459**, 630–638 (2018)
43. A.R. Nimbalkar, N.B. Patil, V.V. Ganbavle, S.V. Mohite, K.V. Madhale, M.G. Patil, Sol-gel derived aluminium doped zinc oxide thin films: a view of aluminium doping effect on physicochemical and NO₂ sensing properties. *J. Alloys Compd.* **775**, 466–473 (2019)
44. Y.H. Zhang, Y.L. Li, F.L. Gong, K.F. Xie, M. Liu, H.L. Zhang, S.M. Fang, Al doped narcissus-like ZnO for enhanced NO₂ sensing performance: an experimental and DFT investigation. *Sens. Actuators B* **305**, 127489 (2020)
45. A. Sanger, S.B. Kang, M.H. Jeong, C.U. Kim, J.M. Baik, K.J. Choi, All-transparent NO₂ gas sensor based on free-standing Al doped ZnO nanofibers. *ACS Appl. Electron. Mater.* **1**, 1261–1268 (2019)
46. J. Hu, C. Zou, Y. Su, M. Li, Y. Han, E.S.-W. Kong, Z. Yang, Y. Zhang, An ultrasensitive NO₂ gas sensor based on a hierarchical Cu₂O/CuO mesocrystal nanoflower. *J. Mater. Chem. A* **6**, 17120–17131 (2018)
47. C. Zhang, A. Boudiba, P. De Marco, R. Snyders, M.G. Olivier, M. Debliquy, Room temperature responses of visible-light illuminated WO₃ sensors to NO₂ in sub-ppm range. *Sens. Actuators B* **181**, 395–401 (2013)
48. O. Casals, N. Markiewicz, C. Fabrega, I. Gracia, C. Cane, H.S. Wasisto, A. Waag, J.D. Prades, A parts per billion (ppb) sensor for NO₂ with microwatt (μW) power requirements based on micro light plates. *ACS Sens.* **4**, 822–826 (2019)
49. J. Berkowitz, W.A. Chupka, D. Gutman, Electron affinities of O₂, O₃, NO, NO₂, NO₃ by endothermic charge transfer. *J. Chem. Phys.* **55**(6), 2733–2745 (1971)
50. L. Liu, H. Hou, L. Wang, R. Xu, Y. Lei, S. Shen, D. Yang, W. Yang, A transparent CdS@TiO₂ nanotextile photoanode with boosted photoelectrocatalytic efficiency and stability. *Nanoscale* **9**, 15650–15657 (2017)

Publisher's Note Springer Nature remains neutral with regard to jurisdictional claims in published maps and institutional affiliations.